Original Article

Effects of nanostructural hierarchy on the hardness and thermal stability of an austenitic stainless steel

Wei Jiang [a], Yang Cao [a,*], Yingda Jiang [b], Yanfang Liu [a], Qingzhong Mao [a], Hao Zhou [a], Xiaozhou Liao [c], Yonghao Zhao [a,*]

[a] Nano and Heterogeneous Materials Center, School of Materials Science and Engineering, Nanjing University of Science and Technology, Nanjing, 210094, China
[b] School of Materials Science and Engineering, Shenyang Ligong University, Shenyang, 110159, China
[c] School of Aerospace, Mechanical and Mechatronic Engineering, The University of Sydney, Sydney, NSW, 2006, Australia

ARTICLE INFO

ABSTRACT

An austenitic stainless steel was processed by high-pressure torsion, and formed a hierarchical nanostructure with ultrafine grains, ultrafine-precipitates, nano-twins and high densities of dislocations. As a result, the hierarchical nanostructure contributes collectively to the double hardness value of the austenitic stainless steel (514 ± 44 HV) in comparison to the coarse-grained counterpart (217 ± 11 HV). Both the nanostructural hierarchy and high hardness can be maintained at the temperatures up to ~600 °C. Annealing treatment at temperatures from 400 to 600 °C may induce recovery to the hierarchical nanostructure, resulting in a reduced microstructural heterogeneity and increased hardness for the high-pressure torsion processed steel.

1. Introduction

Austenitic heat resistant stainless steels offer a resistance to large variation in temperature, thus have wide industrial applications including pipes, furnaces, heat-exchangers, incinerators and steam turbines [1,2]. Nevertheless, the comparatively low specific strength puts a limit on the industrial applications of austenitic stainless steels [3]. Development of thermally stable steels with high strength is of significant importance to both industrial applications and scientific research.

Conventional practice for simultaneously improving strength and thermal resistance requires alloying, nano-clustering and precipitation to suppress static recrystallization and grain growth [4—7]. However, considering the fundamental physics of materials strengthening, it is the activities of defects playing the major role in determining the strength of materials under service conditions [8]. This idea shifts our attention to the manipulation of defects by plastic deformation, in seeking for an austenitic stainless steel with high strength and high thermal stability.

Severe plastic deformation (SPD) is capable of introducing an extremely large amount of defects including dislocations, grain boundaries (GBs) and twin boundaries (TBs), to significantly boost the strength of metallic materials [9,10]. However, not all defects are stable at high temperatures, such as statistical dislocations and high energy GBs [11—13]. According to the classical model of curvature-driven GB migration, the driving force for GB migration increases with decreasing grain size [11,14]; Hence, most of the SPD processed materials with ultrafine grained (UFG) structures are prone to static recrystallization and grain growth upon annealing. In 2012, Yan et al. [15] have demonstrated that nano-twin bundles have superior thermal stability than nano-sized grains in the same material processed by dynamic plastic deformation. In 2016, Zeng et al. [16] processed an ultrafine grained Cu alloy, containing a large amount of secondary phase particles, with an outstanding thermal stability at 1050 °C by a complicated powder metallurgy process.

Inspired by the early work, we have attempted HPT processing to produce an austenitic stainless steel having a hierarchical nanostructure that features ultrafine-precipitates, ultrafine grains, high densities of nano-twins and high densities of dislocations. The nanostructural hierarchy grants the steel with a superior hardness and a high thermal stability at the temperatures up to ~600 °C.

2. Materials and methods

The model material is an austenitic stainless steel supplied by Baoshan Iron & Steel Co., Ltd. Shanghai, China. The austenitic stainless steel is commonly used for making incinerators and steam turbines [1,2]. The as received plates were directly cut from boiler tubes with a final heat treatment at 1000 °C for 10 h before delivery and a dimension of 37 mm inner diameter and 57 mm outer diameter. The working temperature of boiler tubes is in a range of 600650 °C. A summary of the composition of the material is provided in Table 1.

A steel plate was firstly cut into disks with a diameter of ~20 mm and a thickness of ~1.5 mm. The disks were then ground and sequentially polished to obtain a smooth surface and a uniform thickness of ~1.2 mm for HPT processing. The processing was conducted under quasi-constrained conditions [17,18] using an applied pressure of 5.0 GPa, and with the disks processed through 10 revolutions. HPT disks were isochronally annealed for 1 h at temperatures ranging from 400 to 900 °C.

It is known that the shear strain imposed by HPT is a function of the disk radius. In order to minimize the effect of strain variation on microstructures, the position of our investigated sample is about 7 mm away from the center of the HPT disk. Samples for scanning electron microscopy (SEM) characterization and Vickers hardness tests were mechanically polished using 1200 grit SiC papers, 6 and 1 μm diamond papers and 0.4 μm colloidal silica suspensions sequentially. Samples for transmission electron microscopy (TEM) characterization were 3 mm diameter foils prepared by standard machining and electro-polishing methods. The electrolyte contains 25% perchloric acid and 75% acetic acid, the operation voltage is 20 V and the temperature is 20 °C. An automated Bruker-AXS D8 Advance diffractometer with Cu Ka radiation source was used for X-ray diffraction (XRD) analysis. A Carl Zeiss-Auriga SEM was used for electron backscatter diffraction (EBSD) and surface topography analysis. A FEI-Tecnai G2-20-S-TWIN microscope equipped with an Oxford X-Max^N energy dispersive X-ray (EDX) detector, operating at 200 kV, was used for diffraction contrast imaging and EDX analysis. Vickers hardness tests were conducted on a Shimadzu HMV-G hardness tester with a load of 1.961 N and a holding time of 15 s. The choice of the load for the hardness test has to guarantee that the shape of the square-pyramid indent is sharp and clear, and the size of indent is large enough within a range of several tens micrometer in order to minimize the measurement error.

3. Results

According to Table 1, the major alloying elements are 17.1 wt.% Cr, 12.3 wt.% Ni and 2.1 wt.% Cu. Both Cr and Ni are commonly used in making austenitic heat resistant stainless steel with high corrosion resistance and heat resistance [19]. Addition of Cu in steels can improve the antibacterial property and corrosion resistance [20]. The solubility of Cu in iron solvent is less than 1.5 wt.% at the temperature below 700 °C [21]. Therefore, the steels with the Cu contents higher than 1.5 wt.% can form Cu-rich precipitates, and thus can possess precipitation strengthening, even at high service temperatures. In this work, the Cu-rich precipitates were formed at the final heat treatment, at 1000 °C for 10 h before delivery of boiler tubes. This aging temperature is significantly higher than the usual aging temperature (<600 °C) of stainless steels. As a result, the spherical precipitates with an average size of 300 nm embedded in austenite grains are observed, as shown in Fig. 1. The reader should note that the Cu-rich precipitates are intermetallic compounds containing Fe, Cu, Ni and some other elements. The Cu-rich precipitates usually possess a complex core—shell structure which changes in shape and structure with increasing temperature and altered elemental contents. The reader can refer to literatures for details about the Cu-rich precipitates in steels [20,22]. According to the EDX analysis data provided in Table 2, the ultrafine-precipitates are a Cu-rich phase with the Cu content more than three times higher than the nominal Cu content of the steel. Both XRD and EBSD results show only the austenitic phase in the as-received austenitic stainless steel sample (Fig. 2), indicating that the matrix is of a single austenitic phase and the volume fraction of the precipitates is low. According to the EBSD map shown in Fig. 2b, the as-received austenitic stainless steel has a coarse-grained structure with an average grain size of ~23 μm. Annealing twins are randomly observed in the steel. At least 300 grains have been counted for each statistical

Table 1 — Composition of the as-received austenitic stainless steel in wt.%.

Cr	Ni	Cu	Mn	Mo	W	Si	S	C	Fe
17.1	12.3	2.1	0.61	0.02	0.01	0.19	0.01	0.1	Base
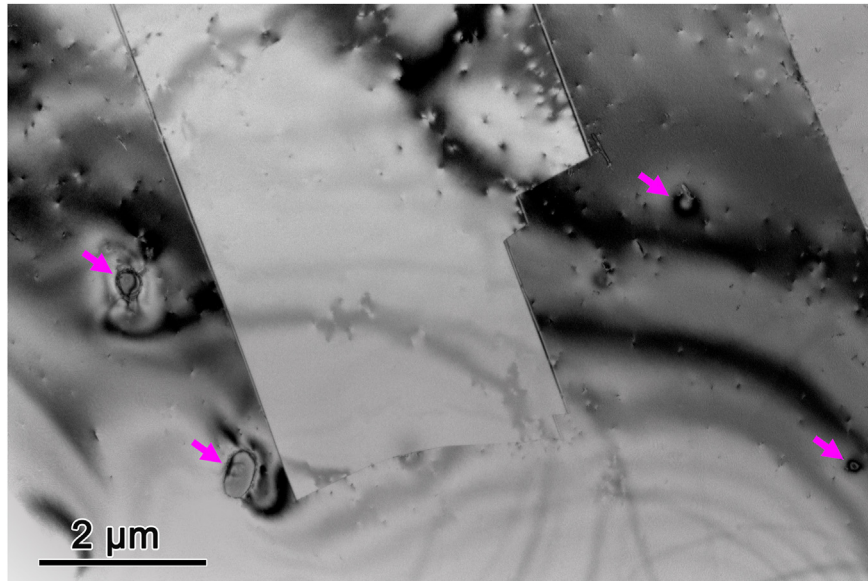
Fig. 1 – An TEM image showing nano-precipitates (marked by orchid arrows) embedded in an austenite grain.

analysis. This rule has been applied to both TEM and EBSD based data analysis throughout this work.

After HPT processing to 10 revolutions, the microstructures in the steel were significantly refined, as shown in Fig. 3. Both nano-twin bundles and ultrafine grains are found in the austenite. The shape, size and density of the Cu-rich precipitates are unchanged compared to the as-received sample, indicating that SPD causes no significant change to the precipitate particles. XRD analysis found that the dislocation density at the area of study is as high as $6.27 \times 10^{14}\,\text{m}^{-2}$ (Table 3). Thus, the HPT steel sample possess a hierarchical nanostructure that is a mixture of ultrafine-precipitates, ultrafine grains, high densities of nano-twins and high densities of dislocations.

After annealing at 500 °C for 1 h, the nanostructure at the area of study of the HPT disk seems unchanged, as shown in Fig. 4a, b and c. The ultrafine sub-grains with irregular shapes and diffuse GBs are still evident in Fig. 4a. A high density of nano-twins even in four twinning systems [23] can be found in Fig. 4b. As shown in Fig. 4c, the boundaries of nano-twins are curved due to severe dislocation-TB intersections [24,25]; A large number of dislocations associated with local strain field distortions are evidenced by non-uniform diffraction contrast in the TEM image. Similar nanostructures are also observed in the HPT samples annealed at 600 °C, hence the hierarchical nanostructure processed by HPT is sustainable at the service temperature below 600 °C. After annealing at 700 °C for 1 h, the microstructures at the area of study displayed some noticeable changes. As shown in Fig. 4d, recrystallized grains (one is labelled RG) containing low densities of dislocations and with

sharp grain boundaries, are found at the UFG region. Meanwhile, twinned regions still contain high densities of nano-twins and dislocations. Thus, clear contrast can be seen between the region of deformation twins (DT) and the region of recrystallized grains (RG) in Fig. 4e. The excess energy of a TB is significantly lower than that of a conventional GB, thus nano-twins have a much better thermal stability than ultrafine grains [11,14,15]. This concept is also supported by Fig. 4f, in which a shear band has recrystallized and surrounding nano-twins are nearly unchanged. As the annealing temperature increased further to 900 °C, significant recovery and recrystallisation transformed the nanostructural hierarchy back to the coarse-grained state with low densities of TBs and dislocations as shown in Fig. 4g. Fig. 5 shows a typical EBSD image and statistical grain size distribution of the sample annealed at 800 °C.

Statistical analysis was conducted based on microstructural data collected by means of TEM, EBSD and XRD. As illustrated in Fig. 6a, the average grain size of the austenitic stainless steel was ~195 nm after HPT processing, and sustained at about 200 nm until the annealing temperature of 600 °C was reached. It is worth noting that the average grain sizes after annealing at 400, 500 and 600 °C was 250, 201 and 262 nm, respectively. It has been widely reported that HPT may introduce microstructural heterogeneity [26,27], thus it is difficult to determine whether the fluctuation in grain sizes was caused by HPT or by annealing yet at this point. Notwithstanding, the UFG region showed strong thermal stability at the annealing temperatures up to 600 °C. In contrast, nano-twins have better thermal stability than ultrafine grain. In fact, the average twin thickness is sustained at about 60 nm until the annealing temperature of 700 °C was reached. Once the thermal stability of nano-twins was breached by the high temperature above 700 °C, thermally induced de-twinning occurred vigorously to cause significant increase in twin thickness as indicated by Fig. 6b. Both EBSD

Table 2 – Composition of a typical nano-precipitate particle in wt.% measured by energy dispersive X-ray analysis.

Cr	Ni	Cu	Mn	Mo	W	Si	S	Fe
19.93	6.12	7.12	0.00	0.00	0.00	0.19	14.52	52.31
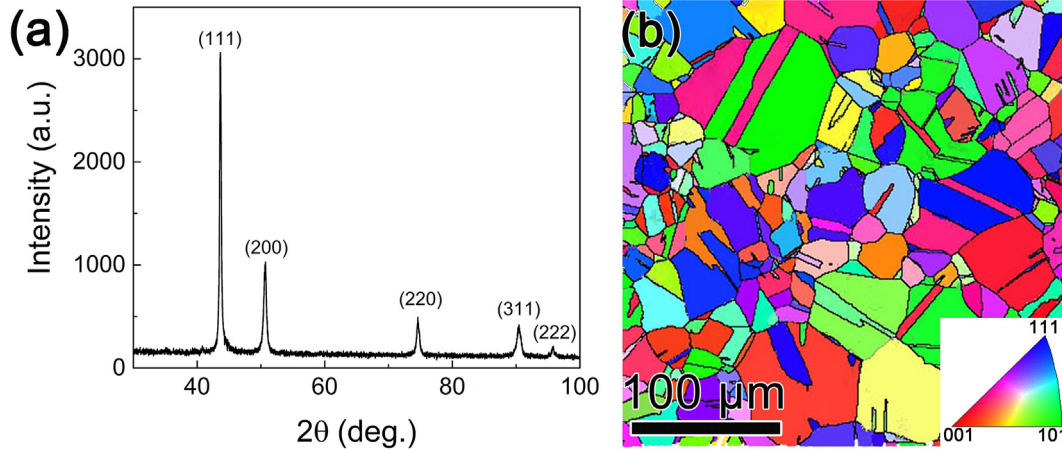
Fig. 2 − (a) An XRD pattern for the as-received austenitic stainless steel; (b) An EBSD map displaying orientations of grains with the Inverse Pole Figure coloring scheme (the color code is given at the bottom right corner).

and XRD data were used to measure dislocation densities. The XRD method is [28]:

$$\rho = \frac{2\sqrt{3}(\varepsilon^2)^{\frac{1}{2}}}{d_{XRD}b} \quad (1)$$

where ε and d_{XRD} is microstrain and grain size which can be obtained by XRD, respectively, b (0.254 nm) is the magnitude of Burgers vector. While the EBSD method is used according to the equation [29]:

$$\rho = \frac{2\theta_{KAM}}{xb} \quad (2)$$

where ρ is the dislocation density, θ_{KAM} is the kernel average misorientation, x is unit length which is equal to twice the step size (70 nm for samples annealed below 700 °C and 100 nm for samples annealed above 700 °C) used in EBSD acquisition. The results in Fig. 6c show that dislocation densities gradually decrease with increasing annealing

temperature, but significant recovery occurred in the temperature range between 600 and 800 °C when the dislocation density (XRD data) dropped sharply from 3.36×10^{14} to 3.0×10^{12} m^{-2}. (Note: the dislocation densities measured by XRD and EBSD are sensitive to different types of instrumental and analytical errors, therefore the trend of dislocation density evolution is more meaningful than the actual numbers shown in Fig. 6c).

Microhardness tests were carried out to investigate the thermal stability of the HPT steel with hierarchical nanostructures. In-depth analysis based on all available hardness and microstructural data reveals that the microstructural evolution with the increasing annealing temperature can be divided into four stages as shown in Fig. 7a. At stage 1 (blue color zone in Fig. 7a), hardness of the HPT steel increases slightly with increasing annealing temperature up to 500 °C. The hardness of HPT steel was 514 HV with a standard deviation of 44 HV. After annealing at 500 °C for 1 h, the hardness
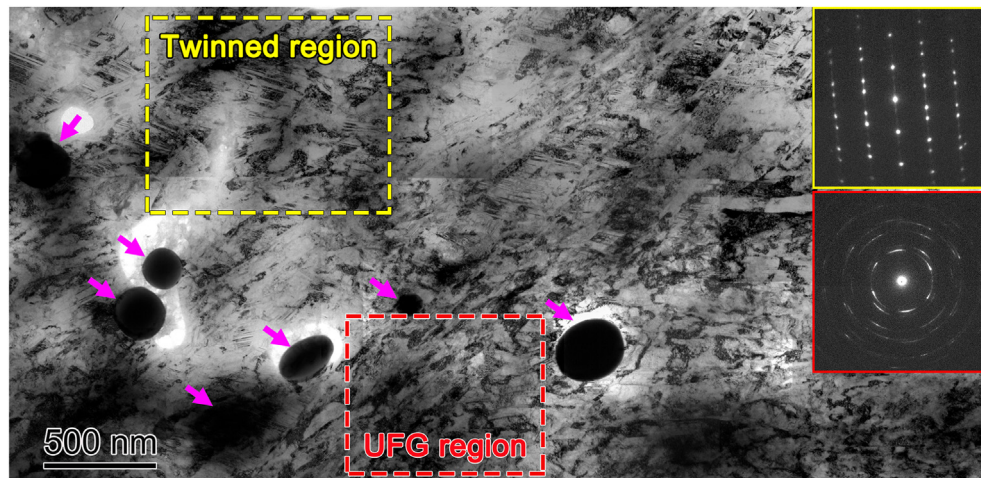
Fig. 3 − The typical microstructure observed at the area of study on the HPT steel disk; Diffraction patterns are obtained from the twinned region and the UFG region, and are given as insets on the right-hand side of this figure; Cu-rich precipitates are marked by orchid arrows.

Table 3 – Hardness and microstructural parameters measured at various annealing temperatures. D – grain size, T – twin thickness, ρ_{XRD} – XRD measured dislocation density, ρ_{EBSD} – EBSD measured dislocation density.

| Temperature (°C)	20, HPT	400	500	600	700	800	900
Hardness (HV)	514 ± 44	530 ± 32	534 ± 27	520 ± 27	387 ± 20	281 ± 21	215 ± 10
D (nm)	195 ± 90	250 ± 110	201 ± 90	262 ± 110	787 ± 340	3399 ± 840	3792 ± 850
T (nm)	53 ± 23	48 ± 26	48 ± 31	64 ± 35	60 ± 27	204 ± 76	447 ± 123
ρ_{XRD} ($\times 10^{14}$ m^{-2})	6.27	4.41	4.01	3.36	0.81	0.03	0.11
ρ_{EBSD} ($\times 10^{14}$ m^{-2})	35.8	24.4	23.8	13.0	3.56	1.99	2.07

of the HPT steel increased to 534 HV with a standard deviation of 27 HV. Moderate increase in hardness indicates that annealing induced hardening occurred [30]; Reduced standard deviation of hardness values indicates that microstructural heterogeneity is reduced. Although TEM images show negligible change in microstructure at the stage 1, moderate decline in dislocation density (Fig. 6c and Table 3) indicates that recovery has occurred during stage 1 annealing. Severely deformed materials are prone to dislocation recovery due to excess amount of dislocations and boundaries [13,30]. For nanostructured materials, recovery will significantly reduce the number of dislocation sources, thus higher yield stress is realized for activating new dislocation sources upon straining [30]. One may argue that, the microstructural changes by recovery are subtle and occur on a very small scale; In addition, austenitic stainless steels with low stacking fault energies (SFEs) are less prone to recovery than high SFE materials [13]. In the HPT steel, dislocation density is very high (6.27×10^{14} m^{-2} measured by XRD and 3.6×10^{15} m^{-2} measured by EBSD) and Cu-rich ultrafine-precipitates are at present. These two microstructural features are the major driving kinetics for dislocation recovery. Thus, noticeable recovery could occur before recrystallisation, leading to the moderate increase in hardness during annealing at the stage 1. Moreover, the decrease in microstructural heterogeneity (indicated by reduced standard deviation in hardness) is another strong evidence for static recovery. The grains with higher dislocation densities would undergo more pronounced recovery. As a result, the difference in dislocation density among most of the grains are reduced, leading to a reduced microstructural heterogeneity.

At stage 2 (aqua color zone in Fig. 7a), hardness of the HPT steel decreases sharply with increasing annealing temperature from 600 to 700 °C. Grain growth in the UFG region and overall decrease in dislocation density are the major contributors to the hardness drop. In contrast, the average twin thickness is nearly unchanged at this stage, therefore the hardness is still significantly higher than the coarse-grained counterpart. At stage 3 (green color zone in Fig. 7a), hardness of the HPT steel continues to decrease sharply with increasing annealing temperature from 700 to 800 °C. At this stage, the thermal stability of the HPT steel cannot maintain. Significant recovery and recrystallisation occurred to increase the grain sizes back to the coarse-grained regime, to decrease both dislocation density and twin density, and to increase the average twin thickness to ~204 nm. At stage 4 (white color zone in Fig. 7a), the microstructure gradually evolves to an equilibrium state that is similar to the as-received austenitic stainless steel. As a result, hardness of the HPT steel annealed at 900 °C is comparable to the as-received sample.

4.   Discussion

The hardness and the thermal stability of the HPT steel are compared to other nanostructured steels in Fig. 7b [5,31–41].
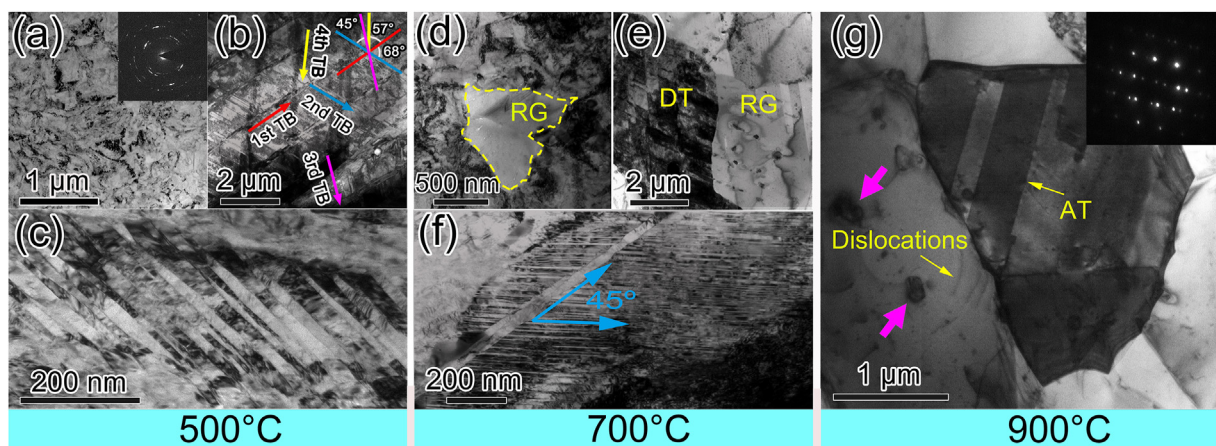
Fig. 4 – TEM images showing typical microstructures of the HPT steel sample annealed for 1 h, at 500 °C, 700 °C, 900 °C: (a) UFG structure, (b) deformation twins in multiple systems, (c) magnified image of deformation twins, (d) a partially recrystallized grain (RG), (e) recrystallized grains and deformation twins (DT), (f) a high density of nano-twins with a recrystallized shear band, and (g) recrystallized coarse grains.
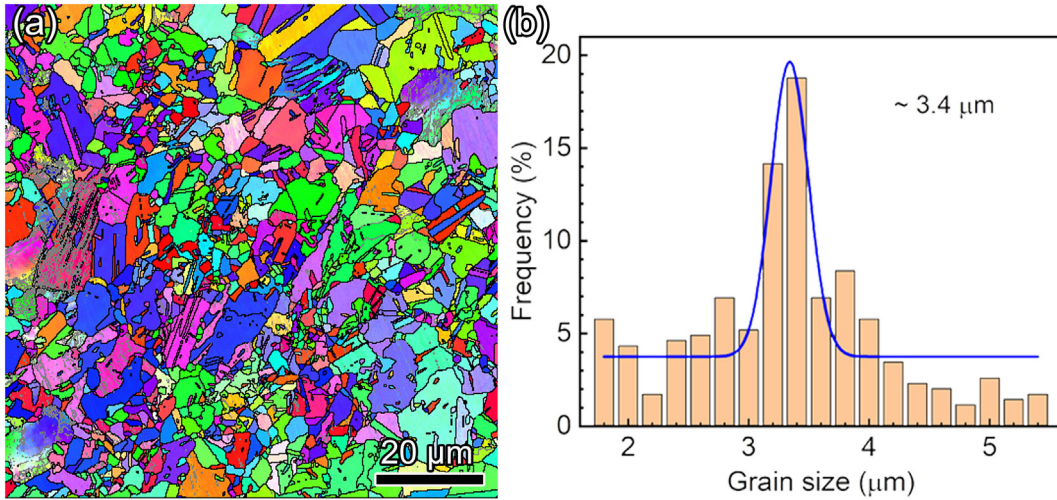
Fig. 5 — EBSD image and statistical grain size distribution of the sample annealed at 800 °C.

Among conventional alloys, steels show superior hardness and specific strength. In current work, hardness of the HPT steel is significantly higher than other types of steels when its hierarchical nanostructure is sustained below 600 °C. This is because among all UFG steels compared in Fig. 7b, HPT steel has the smallest average grain size and highest twin density, and stable Cu-rich precipitates. However, smaller grain size may lead to an issue of increased tendency for grain growth during annealing. The grain size effect on the kinetics of sub-grain growth is described by the Arrhenius relationship [13,38]:

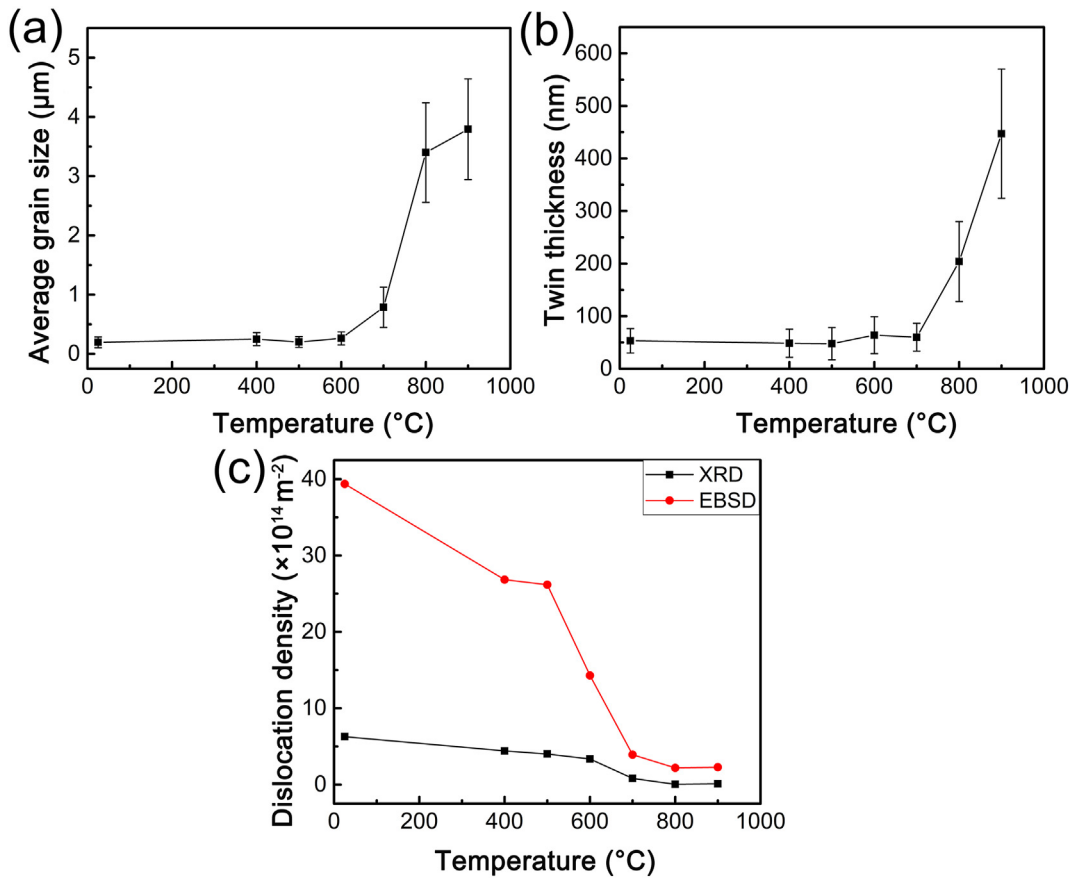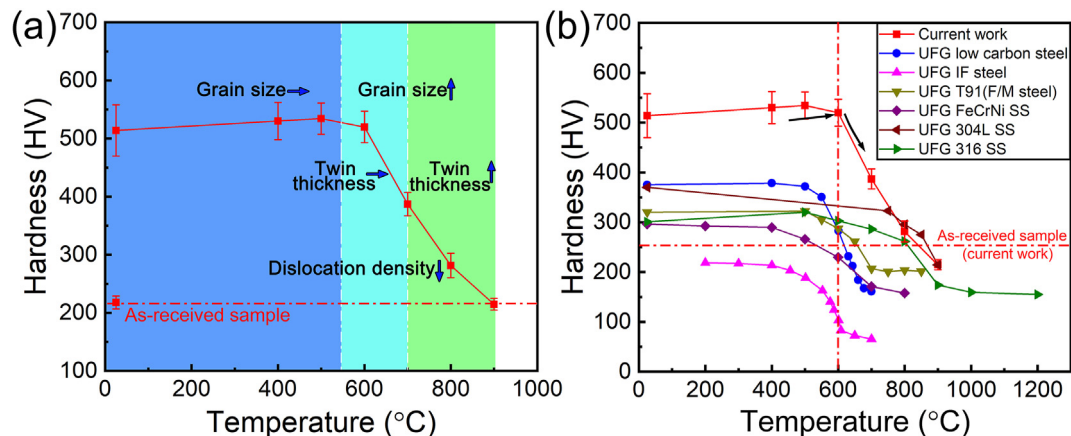$$d^n - d_0^n = tK_0 \exp\left(-\frac{Q}{RT}\right) \tag{3}$$

Fig. 6 — Charts illustrating (a) average grain size vs. temperature, (b) twin thickness vs. temperature, and (c) dislocation density vs. temperature.

Fig. 7 − (a) Hardness evolution with respect to the annealing temperature for the HPT steel; (b) Comparison of hardness evolutions with respect to varying annealing temperatures for NG and UFG materials.

where d is the grain size after grain growth, d_0 is the grain size prior to grain growth, n is the grain growth exponent, t is the annealing time, K_0 is a constant; Q is the activation energy for grain growth, R is the gas constant, and T is the annealing temperature. The value of n is affected by composition and temperature. According to the literature [13], n for an austenitic stainless steel is in the range between ~4.54 and ~7.14. If a medium value of $n = $~5.55 is used for the estimation, by plotting $ln\ (d^n - \ d_0^n)$ vs. $1/T$, an activation energy of $Q = 461.8$ kJ/mol for grain growth can be extracted from the slope. All other steels surveyed in Fig. 7b [5,37−39,41] have activation energies for grain growth in the range between 207 and 475 kJ/mol. The activation energy for grain growth in the HPT steel is at the upper bond in comparison to those commonly studied steels. Therefore, the thermally stable ultrafine grains are the major contributor to the overall thermal stability of the HPT steel.

In fact, a comparison of the turning points on the hardness vs. temperature curves (Fig. 7b) provides another direct evidence of the high thermal stability of the HPT steel. The term "turning point" used here is the annealing onset temperature at which hardness begins to decline. For example, the turning point for the HPT steel is at 590 °C; To the right of the turning point, a sharp drop in the hardness of the HPT steel is realized. A vertical dashed line is drawn across the turning point of the HPT steel at 590 °C as a reference line in Fig. 7b. In contrast, for the IF steel [36], T91 steel [37], FeCrNi stainless steel [38] and low carbon steel [35], the turning points are all clearly (located to the left of the dashed line) below 600 °C. Thus, it can be concluded that the HPT steel with a hierarchical nanostructure is thermally more stable than those UFG steels. However, the turning points of the 304 L [39,41] and 316 stainless steel [5] are approximately (located to the right of the dashed line) at 700 °C which is higher than the HPT steel. The better thermal stability of 304 L is attributed to a larger average grain size of 650 nm and higher content of Mo and V [39,41]. The high thermal stability of 316 stainless steel is attributed to the coarse-grained structure and stable nano-twins.

The strength and thermal stability of a nanostructured material are determined by the combined effect of grain size, GBs, nano-twins, alloying elements, dislocation density, precipitates, texture, SFE and microstructural heterogeneity. The high hardness and high thermal stability of the HPT steel revealed by Fig. 7b suggests that the nanostructural hierarchy shown in Fig. 3 is effective in improving materials mechanical properties. However, in-depth analysis based on current result and literature surveys suggests that further improvements to materials properties are still possible. For example, nano-grains in a Cu-12at%Al alloy can be stabilized by the presence of nanoscale Cu−Al intermetallic precipitates at 900 °C [31]. For another example, nano-twins show stability at 800 °C in coarse grained 316 stainless steel [5] and in UFG Cu [42]. Thus, our future work will focus on manipulating intrinsic properties and processing conditions to promote nano-twins and nano-precipitates to further improve the strength and thermal stabilities of steels.

5. Conclusions

In conclusion, an austenitic stainless steel with hierarchical nanostructure featuring Cu-rich precipitates, ultrafine grains, high densities of nano-twins and high densities of dislocations, has been processed by HPT. The HPT steel possesses a high hardness which is sustainable above 500 HV after annealing at 600 °C for 1 h. Annealing at 500 °C for 1 h can moderately increase the hardness and reduce the microstructural heterogeneity of the HPT steel, indicating that moderate recovery is helpful for sustaining the high hardness of a nanostructured steel processed by SPD.

Author's contribution

Wei Jiang did TEM, EBSD, heat-treatment and hardness experiments. Wei' Jiang wrote the first draft of the paper. Yingda Jiang did composition analysis. Xiaozhou Liao provided the HPT equipment and did HPT processing. Yanfang Liu assisted with TEM analysis. Qingzhong Mao did XRD experiment. Hao

Zhou did EDX analysis. Yang Cao and Yonghao Zhao designed and coordinated the project and revised the paper.

Declaration of Competing Interest

The authors declare that they have no known competing financial interests or personal relationships that could have appeared to influence the work reported in this paper.

Acknowledgements

REFERENCES

[1] Zhao CZ, Wei SS, Gao YL, Wang YH. Progress of heat resistant steel for supercritical and ultra supercritical steam turbine. J Iron Steel Res 2007;19:1–5.

[2] Masuyama F. Advances in physical metallurgy and processing of steels. History of power plants and progress in heat resistant steels. ISIJ Int 2001;41:612–25.

[3] Baddoo NR. Stainless steel in construction: a review of research, applications, challenges and opportunities. J Constr Steel Res 2008;64:1199–206.

[4] Islamgaliev RK, Valiev RZ, Misha RS, Mukherjee AK. Enhanced superplastic properties in bulk metastable nanostructured alloys. Mater Sci Eng, A 2001;304:206–10.

[5] Wang SJ, Jozaghi T, Karaman I, Arroyave R, Chumlyakov YI. Hierarchical evolution and thermal stability of microstructure with deformation twins in 316 stainless steel. Mater Sci Eng, A 2017;694:121–31.

[6] Koch CC, Scattergood RO, Darling KA, Semones JE. Stabilization of nanocrystalline grain sizes by solute additions. J Mater Sci 2008;43:7264–72.

[7] Li LL, Saber M, Xu WZ, Zhu YT, Koch CC, Scattergood RO. High-temperature grain size stabilization of nanocrystalline Fe–Cr alloys with Hf additions. Mater Sci Eng, A 2014;613:289–95.

[8] Li XY, Lu K. Playing with defects in metals. Nat Mater 2017;16:700–1.

[9] Cao Y, Ni S, Liao XZ, Song M, Zhu YT. Structural evolutions of metallic materials processed by severe plastic deformation. Mater Sci Eng R 2018;133:1–59.

[10] An XH, Wu SD, Wang ZG, Zhang ZF. Significance of stacking fault energy in bulk nanostructured materials: insights from Cu and its binary alloys as model systems. Prog Mater Sci 2019;101:1–45.

[11] Zhou X, Li XY, Lu K. Stabilizing nanograins in metals with grain boundary relaxation. Scr Mater 2020;187:345–9.

[12] Ashby MF. The deformation of plastically non-homogeneous materials. Philos Mag A 1970;21:399–424.

[13] Humpheys FJ, Hatherly M. Recrystallization and related annealing phenomena. 2nd. Oxford: Elsevier; 2004.

[14] Lin YJ, Wen HM, Li Y, Wen B, Liu W, Lavernia EJ. An analytical model for stress-induced grain growth in the presence of both second-phase particles and solute segregation at grain boundaries. Acta Mater 2015;82:304–15.

[15] Yan FK, Liu GZ, Tao NR, Lu K. Strength and ductility of 316L austenitic stainless steel strengthened by nano-scale twin bundles. Acta Mater 2012;60:1059–71.

[16] Zeng W, Zheng DQ, Li HM, Zhou DS, Zhang DL. Using intragranular and intergranular second phase particles simultaneously to achieve high temperature stabilization of ultrafine grained Cu. Mater Sci Eng, A 2016;670:41–8.

[17] Zhilyaev AP, Langdon TG. Using high-pressure torsion for metal processing: fundamentals and applications. Prog Mater Sci 2008;53:893–979.

[18] An XH, Lin QY, Sha G, Huang MX, Ringer SP, Zhu YT, et al. Microstructural evolution and phase transformation in twinning-induced plasticity steel induced by high-pressure torsion. Acta Mater 2016;109:300–13.

[19] Zhou YH, Liu YC, Zhou XS, Liu CX, Yu JX, Huang Y, et al. Precipitation and hot deformation behavior of austenitic heat-resistant steels: a review. J Mater Sci Technol 2017;33:1448–56.

[20] Shi XB, Yan W, Xu DK, Yan MC, Yang CG, Shan YY, et al. Microbial corrosion resistance of a novel Cu-bearing pipeline steel. J Mater Sci Technol 2018;34:2480–91.

[21] Ren L, Zhu JM, Nan L, Yang K. Differential scanning calorimetry analysis on Cu precipitation in a high Cu austenitic stainless stee. Mater Des 2011;32:3980–5.

[22] Wen YR, Li YP, Hirata A, Zhang Y, Fujita T, Furuhara T, et al. Synergistic alloying effect on microstructural evolution and mechanical properties of Cu precipitation-strengthened ferritic alloys. Acta Mater 2013;61:7726–40.

[23] Liu XW, Sun LG, Zhu LL, Liu JB, Lu K, Lu J. High-order hierarchical nanotwins with superior strength and ductility. Acta Mater 2018;149:397–406.

[24] Cao Y, Wang YB, An XH, Liao XZ, Kawasaki M, Ringer SP, et al. Grain boundary formation by remnant dislocations from the de-twinning of thin nano-twins. Scr Mater 2015;100:98–101.

[25] Cao Y, Wang YB, An XH, Liao XZ, Kawasaki M, Ringer SP, et al. Concurrent microstructural evolution of ferrite and austenite in a duplex stainless steel processed by high-pressure torsion. Acta Mater 2014;63:16–29.

[26] Cao Y, Wang YB, Figueiredo RB, Chang L, Liao XZ, Kawasaki M, et al. Three-dimensional shear-strain patterns induced by high-pressure torsion and their impact on hardness evolution. Acta Mater 2011;59:3903–14.

[27] Jiang W, Zhou H, Cao Y, Nie JF, Li YS, Zhao YH, et al. On the heterogeneity of local shear strain induced by high-pressure torsion. Adv Eng Mater 2020;22:1900477.

[28] Bakshi SD, Sinha D, Chowdhury SG. Anisotropic broadening of XRD peaks of α′-Fe: williamson-Hall and Warren-Averbach analysis using full width at half maximum (FWHM) and integral breadth(IB). Mater Char 2018;142:144–53.

[29] Liu YF, Cao Y, Mao QZ, Zhou H, Zhao YH, Jiang W, et al. Critical microstructures and defects in heterostructured materials and their effects on mechanical properties. Acta Mater 2020;189:129–44.

[30] Huang XX, Hansen N, Tsuji N. Hardening by annealing and softening by deformation in nanostructured metals. Science 2006;312:249–51.

[31] Chakravarty S, Sikdar K, Singh SS, Roy D, Koch CC. Grain size stabilization and strengthening of cryomilled nanostructured Cu 12 at% Al alloy. J Alloys Compd 2017;716:197–203.

[32] Li ZM, Fu LM, Fu B, Shan AD. Effects of annealing on microstructure and mechanical properties of nano-grained titanium produced by combination of asymmetric and symmetric rolling. Mater Sci Eng, A 2012;558:309—18.

[33] Tang LL, Zhao YH, Islamgaliev RK, Valiev RZ, Zhu YT. Microstructure and thermal stability of nanocrystalline Mg-Gd-Y-Zr alloy processed by high pressure torsion. J Alloys Compd 2017;721:577—85.

[34] Suo T, Li YL, Xie K, Zhao F, Zhang KS, Deng Q. Experimental investigation on strain rate sensitivity of ultra-fine grained copper at elevated temperatures. Mech Mater 2011;43:111—8.

[35] Maier GG, Astafurova EG, Maier HJ, Naydenkin EV, Raab GI, Odessky PD, et al. Annealing behavior of ultrafine grained structure in low-carbon steel produced by equal channel angular pressing. Mater Sci Eng, A 2013;581:104—7.

[36] Niendorf T, Maier HJ, Canadinc D, Karaman I. Cyclic stability of ultrafine-grained interstitial-free steel at elevated temperatures. Mater Sci Eng, A 2009;503:160—2.

[37] Hao T, Fan ZQ, Zhao SX, Luo GN, Liu CS, Fang QF. Strengthening mechanism and thermal stability of severely deformed ferritic/martensitic steel. Mater Sci Eng, A 2014;596:244—9.

[38] Sun C, Yang Y, Liu Y, Hartwig KT, Wang H, Maloy SA, et al. Thermal stability of ultrafine grained Fe—Cr—Ni alloy. Mater Sci Eng, A 2012;542:64—70.

[39] Sabooni S, Karimzadeh F, Enayati MH. Thermal stability study of ultrafine grained 304L stainless steel produced by martensitic process. J Mater Eng Perform 2014;23:1665—72.

[40] An XH, Wu SD, Zhang ZF, Figueiredo RB, Gao N, Langdon TG. Enhanced strength-ductility synergy in nanostructured Cu and Cu-Al alloys processed by high-pressure torsion and subsequent annealing. Scr Mater 2012;66:227—30.

[41] Marchattiwar A, Sarkar A, Chakravartty JK, Kashyap BP. Dynamic recrystallization during hot deformation of 304 austenitic stainless steel. J Mater Eng Perform 2013;22:2168—75.

[42] Anderoglu O, Misra A, Wang H, Zhang X. Thermal stability of sputtered Cu films with nanoscale growth twins. J Appl Phys 2008;103:1357.